UniScatter: Unifying Backscatter Communications, Symbiotic Radio, and Reconfigurable Intelligent Surface

Yang Zhao, *Member, IEEE,* and Bruno Clerckx, *Fellow, IEEE*

Abstract—Scatterers can harvest energy from, modulate information over, and influence propagation of surrounding radio waves. Backscatter Communications (BackCom) varies object impedance to manipulate the magnitude, phase, and/or frequency of scattered signal to encode information and deliver within coverage. Reconfigurable Intelligent Surface (RIS) adapts scattering antennas or programmable metamaterial to control wireless propagation environment by boosting/suppressing signal strength in specific directions. Symbiotic Radio (SR) incorporates scatter nodes into active networks that recycle ambient signal to transmit self information and enhance legacy channel to the cooperative receiver. In this paper, we depart from those concepts and introduce UniScatter as a new paradigm for future wireless networks. Instead of treating probability distribution of reflection states as equiprobable (as scattering source of BackCom/SR) or degenerate (as reflecting element of RIS), UniScatter node adapts input distribution of a passive scatter node based on link priority and Channel State Information (CSI), balancing information encoding and channel reconfiguration in a flexible and mutualistic manner. To accommodate signal characteristics, UniScatter receiver semi-coherently decodes all nodes from accumulated energy, acquires equivalent primary channel over reflection pattern, then coherently decodes the primary link under enhanced multipath. It reduces the complexity of cooperative decoding while preserves the benefits of backscatter modulation and passive beamforming. Using shared spectrum, energy, and infrastructures, UniScatter is a more general and powerful transmit-assist protocol that generalizes BackCom, RIS and SR with universal hardware design and augmented Quality of Service (QoS) control. We consider an application scenario where a multi-antenna Access Point (AP) serves a single-antenna user surrounded by multiple UniScatter nodes, and characterize the achievable primary-(total-)backscatter rate region by designing input distribution at the nodes, active beamforming at the AP, and backscatter decision design at the user. Simulation results demonstrate UniScatter nodes can flexibly control the transmit-assist tradeoff via smart input distribution design.

I. Introduction

FUTURE wireless network is envisioned to provide high throughput, uniform coverage, pervasive connectivity, heterogeneous control, and cognitive intelligence for trillions of portable devices. As an emerging low-power communication technique, Backscatter Communications (BackCom) separates conventional transmitter into a Radio-Frequency (RF) emitter with power-hungry elements (e.g., synthesizer and amplifier), and an information-bearing node with power-efficient components (e.g., harvester and modulator) [1]. The node harvests energy from incident wave and embeds information over scattered

The authors are with the Department of Electrical and Electronic Engineering, Imperial College London, London SW7 2AZ, U.K. (e-mail: {yang.zhao18, b.clerckx}@imperial.ac.uk).

signal in a sustainable and controllable manner. The backscatter reader can be either co-located or separated with the emitter, known as monostatic and bistatic BackCom. Its applications such as Radio-Frequency Identification (RFID) [2], [3] and sensor networks [4], [5] have been extensively researched, standardized, and commercialized to support Internet of Things (IoT) and Machine to Machine (M2M). However, traditional BackCom requires dedicated carrier emitter and backscatter reader, while passive nodes only respond when externally inquired. In Ambient Backscatter Communications (AmBC) [6], interactive nodes recycle ambient signals generated by legacy transmitters (e.g., radio, television, and Wi-Fi) to harvest energy and establish connection. It eliminates the need of dedicated power source, carrier emitter, and frequency spectrum, bringing more opportunities to low-power communications. To combat the strong direct-link interference of AmBC, [7] proposed a co-located receiver that cooperatively decodes the primary (legacy) and backscatter links. The authors evaluated the error performance of Maximum-Likelihood (ML), linear, and Successive Interference Cancellation (SIC) detectors for flat fading channel, and proposed a low-complexity detector for frequency-selective fading channel. The concept of cooperative AmBC was then refined as Symbiotic Radio (SR) to cognitively incorporate AmBC with existing systems [8]. In SR, the primary transmitter generates active radio carrying primary information, the secondary node modulates scattered component with backscatter information, and the cooperative receiver decodes both links from two propagation paths. The direct transmitter-receiver path only contains primary information, while the cascaded transmitter-node-receiver path preserves both information due to backscatter principles. Such a coexistence was further classified into commensal, parasitic, and competitive relationships based on link priority [9], and their instantaneous rates, optimal power allocations, and outage probabilities were subsequently derived in [9], [10]. However, one important issue of SR is practical cooperative receiver design. Ideal joint ML decoding achieves optimal performance with prohibitive computational complexity [7], [11]. Due to physical constraints at the load-switching modulator, backscatter symbol period is typically longer than primary. For sequential decoding from primary to backscatter, [12] pointed out the randomness from backscatter modulation can be modelled as either interference or channel uncertainty, depending on symbol period ratio. The authors concluded if this ratio is sufficiently large, the non-coherent primary achievable rate would asymptotically approach its coherent counterpart. This motivated [7], [10]–

[19] to decode the primary link, perform SIC, then decode the backscatter link. However, the advantage of SIC is questionable because 1) backscatter pattern and signal characteristics are not fully exploited; 2) primary rate analysis considers moderately long backscatter symbol period that constraints backscatter rate; 3) non-coherent primary encoding is required at the transmitter, while re-encoding, precoding, and subtraction are required at the receiver; 4) primary and backscatter symbols are mixed by multiplication instead of superposition. Another open issue for SR is backscatter multiple access. [15] proposed a backscatter Non-Orthogonal Multiple Access (NOMA)-based SR by extending SIC to multi-node scenario, where the decoding order depends on backscatter signal strength. However, its performance deteriorates fast when the number of nodes increases. Backscatter Time-Division Multiple Access (TDMA) was also evaluated in [16], where each node transmits information during its own slot and harvests energy during others. Although energy efficiency can be enhanced by transmission time and reflection ratio design, it requires regular feedback to passive nodes and incurs high coordination cost. [20] controls the load-switching speed at nodes to shift the scattered signal to desired frequency bands, which enables backscatter Frequency-Division Multiple Access (FDMA) at the cost of extra bandwidth and higher power consumption. To reduce coordination between passive nodes, [17] proposed a random code-assisted multiple access for SR and evaluated the asymptotic Signal-to-Interference-plus-Noise Ratio (SINR) using random matrix theory. However, it suffers from imperfect synchronization and the near-far problem.

On the other hand, Reconfigurable Intelligent Surface (RIS) is a promising technology that evolves wireless propagation environment using numerous passive reflecting elements (e.g., scattering antenna or programmable metamaterial) with adjustable amplitudes and/or phases [21]. The scattered signals contain no additional information, but adds constructively or destructively with the direct component to enhance desired signal or suppress interference, improving spectrum and energy efficiency. Compared with backscatter nodes of BackCom and SR, the reflection pattern of RIS elements are deterministic and priorly known at transmitter and receiver. It motivated the use of fixed reflection pattern during each channel block to improve communication, sensing, and power performances [22]–[27]. The concept of dynamic RIS, namely choosing independent reflection coefficients for different time slots within channel block, was first proposed to assist Orthogonal Frequency-Division Multiplexing (OFDM) systems [28], then extended for the downlink power and uplink information phases of Wireless Powered Communication Network (WPCN) [29]–[31]. Dynamic RIS introduced artificial channel diversity and flexible resource allocation, but missed the opportunity to encode its own message. From an information-theoretic perspective, [32] reported using RIS as an auxiliary equipment to maximize the Signal-to-Noise Ratio (SNR) is generally rate-suboptimal for finite input constellations. Instead, joint transmitter-RIS encoding achieves the capacity of RIS-aided channel, while layered encoding with SIC decoding (i.e., SIC-based SR) can outperform pure passive beamforming at high SNR. Further attempts

How to combine backscatter modulation and passive beamforming

Although dynamic passive beamforming artificially creates temporal diversity for flexible channel reconfiguration and resource allocation, it demands additional computational cost and control overhead, and the tradeoff deserves further attention especially for large RIS. In [33], [34], RIS was also introduced to single- and multi-node SR systems to reduce the total transmit power. When joint transmitter-RIS encoding is possible, [32] proved using RIS only for passive beamforming is generally suboptimal in terms of achievable rate for finite input constellations. Recently, RIS-empowered SR was introduced in [18], [19], [35] where independent passive beamforming and backscatter encoding were combined using advanced architectures. The authors of [18], [19] proposed the RIS to modulate binary message over the whole phase shift matrix and the receiver to decodes from (non-coherent) primary to (coherent) backscatter link. In contrast, [35] divided the RIS into reflection and information elements, and evaluated the error performance of non-coherent backscatter detection.

Besides, [28] proposed a dynamic passive beamforming that further adjusts RIS over fine-grained time slots for OFDM systems to balance beamforming gain and multiuser diversity. The idea was further applied to WPCN to accommodate the downlink Wireless Power Transfer (WPT) phase and uplink Wireless Information Transfer (WIT) phase of the "harvest-then-transmit" protocol [30], [31]. For multiuser WPT, [36] also reported that dynamic beamforming can mimic multi-beam reflection in a time-division manner and reduce the phase extraction loss. Although dynamic passive beamforming artificially creates temporal diversity for flexible channel reconfiguration and resource allocation, it demands additional computational cost and control overhead, and the tradeoff deserves further attention especially for large RIS. In [33], [34], RIS was also introduced to single- and multi-node SR systems to reduce the total transmit power. When joint transmitter-RIS encoding is possible, [32] proved using RIS only for passive beamforming is generally suboptimal in terms of achievable rate for finite input constellations. Recently, RIS-empowered SR was introduced in [18], [19], [35] where independent passive beamforming and backscatter encoding were combined using advanced architectures. The authors of [18], [19] proposed the RIS to modulate binary message over the whole phase shift matrix and the receiver to decodes from (non-coherent) primary to (coherent) backscatter link. In contrast, [35] divided the RIS into reflection and information elements, and evaluated the error performance of non-coherent backscatter detection.

To the best of our knowledge, all existing SR literatures assumed backscatter modulation employs either Gaussian codebook [9], [10], [12]–[16] or finite equiprobable inputs [7], [11], [17]–[19], [35]. The former is impractical for passive nodes with constrained number of states, while the latter does not fully exploit Channel State Information (CSI) to boost achievable backscatter rate. Besides, most relevant designs [7], [9]–[19] were built over ideal ML or SIC receiver. However, the advantage of SIC is questionable because 1) it requires non-coherent primary encoding at the transmitter and re-encoding, precoding, and subtraction at the receiver, 2) the primary and backscatter symbols are mixed by multiplication

instead of superposition, and 3) the backscatter symbol period is typically much longer due to physical constraints. Motivated by those, we propose the concept of Metascatter, which adapts the input distribution of a passive backscatter node to generalize backscatter sources of SR and reflecting elements of RIS. The contributions of this paper is summarized as follows.

First, Metascatter adapts the input probability distribution of a finite-state passive backscatter device based on primary and (cascaded) backscatter CSI to unify and generalize parasitic source of SR and reflecting elements of RIS. The reflection pattern over time is no longer fully random or deterministic, but can be flexibly distributed to balance backscatter encoding and passive beamforming. For single-user scenario, when primary link is absolutely prioritized, the distribution falls on one state and Metascatter boils down to conventional RIS. When only considering backscatter performance, the distribution involves the highest entropy and Metascatter is essentially an AmBC node.

Second, we consider an application scenario where multiple Metascatters ride over a point-to-point transmission, exploiting additional propagation paths to simultaneously transmit and assist. To fully accommodate backscatter characteristics, we also propose a novel receiving strategy that first jointly decodes all Metascatter from accumulated energy, then models their reflection patterns and backscatter paths within equivalent channel for primary decoding. Since backscatter message is modulated over primary signal, backscatter decoding is indeed part of primary channel training, and there is no need for operation-intensive SIC at the receiver.

Third, we evaluate the achievable primary-(total-)backscatter rate region by optimizing the input distribution at Metascatters, the active beamforming at the Access Point (AP), and the decision regions at the user. Since the original problem is highly non-convex, we consider a suboptimal Block Coordinate Descent (BCD) algorithm where the Karush-Kuhn-Tucker (KKT) input distribution is numerically evaluated by limit of sequences, the active beamforming is iteratively updated by Projected Gradient Descent (PGD) accelerated by backtracking line search, and the decision regions are first restricted to convex, then refined by existing thresholding designs.

Notations: Scalars, vectors and matrices are respectively denoted by italic, bold lower-case, and bold upper-case letters. j represents the imaginary unit. $\mathbb{R}_+^{x \times y}$ and $\mathbb{C}^{x \times y}$ respectively denote the space of real nonnegative and complex $x \times y$ matrices. $\Delta^n = \left\{ (p_0,...,p_n) \in \mathbb{R}_+^{n+1} | \sum_{i=0}^n t_i = 1 \right\}$ denotes the standard n-simplex. $(\cdot)^*$, $(\cdot)^T$, $(\cdot)^H$, $(\cdot)^+$, $|\cdot|$, $\|\cdot\|$ respectively represent the conjugate, transpose, conjugate transpose, ramp function, absolute value, and Euclidean norm. The distribution of a CSCG random vector with mean $\mathbf{0}$ and covariance $\boldsymbol{\Sigma}$ is denoted by $\mathcal{CN}(\mathbf{0}, \boldsymbol{\Sigma})$. $\sim$ means "distributed as". $(\cdot)^{(i)}$ represents the i-th iterated value and $(\cdot)^\star$ represents the end solution.

II. BACKSCATTER PRINCIPLES

Passive backscatter nodes harvest energy from and modulate information over surrounding RF signals. As shown in Fig. 1(a), a typical passive node consists of a scattering antenna, an energy harvester, an integrated receiver, a load-switching modulator, and on-chip components (e.g., micro-controller and sensors) [2]. Its equivalent circuit is presented in Fig. 1(b). When illuminated, the node absorbs a portion of the impinging wave for information decoding and/or energy harvesting [38], and backscatters the remaining as *structural* and *antenna* components. The former consistently contributes to environment multipath and can be modelled by channel estimation [1], while the latter depends on antenna-load impedance mismatch and can be used for backscatter modulation [39] and/or channel reconfiguration [21]. Fig. 1(c) illustrates the scatter model of a node with M states, where the reflection coefficient of state $m \in \mathcal{M} \triangleq \{1,...,M\}$ is defined as[1]

$$\Gamma_m = \frac{Z_m - Z_{\mathrm{A}}^*}{Z_m + Z_{\mathrm{A}}}, \tag{1}$$

where Z_m is the load impedance at state m and Z_{A} is the antenna input impedance.

A. SR: Backscatter Modulation

Backscatter sources encode self message by *random reflection states variation.* For M-ary Quadrature Amplitude Modulation (QAM), reflection coefficient Γ_m maps to the corresponding *complex constellation point* c_m by [40]

$$\Gamma_m = \alpha \frac{c_m}{\max_{m'} |c_{m'}|}, \tag{2}$$

where $0 \le \alpha \le 1$ is the amplitude reflect ratio that controls the harvest-scatter tradeoff at the direction of interest.

B. IRS: Channel Reconfiguration

RIS elements assist legacy transmission by *deterministic phase shifts selection* based on relevant CSI. For a reflecting element with M candidate states, reflection coefficient Γ_m relates to the corresponding *phase shift* θ_m by [22]

$$\Gamma_m = \beta_m \exp(j\theta_m), \tag{3}$$

where $0 \le \beta_m \le 1$ is overall amplitude reflect ratio of state m.

C. Metascatter: Bridge and Generalization

Metascatters simultaneously transmit and assist by *adaptive input distribution design* based on primary and (cascaded) backscatter CSI. Instead of using fully random or deterministic reflection pattern over time, as shown in Fig. 2, Metascatter semi-randomly selects reflection state for each backscatter block, with *guidance of input probability* $P(\Gamma_m)$ for state m. In other words, it flexibly controls input distribution of candidate reflection states to balance backscatter encoding and passive beamforming. SR and RIS can be regarded as extreme cases of Metascatter, where node input distribution boils down to uniform and deterministic, respectively.

Remark 1. *Compared to conventional RIS literatures that optimize phase shifts under unit-module constraint, Metascatter starts from predefined reflection coefficients and designs their input distribution under sum-probability constraint to achieve flexible primary-backscatter tradeoff.*

---

[1]It corresponds to a linear backscatter model where the reflection coefficient is irrelevant to incident electromagnetic field strength.

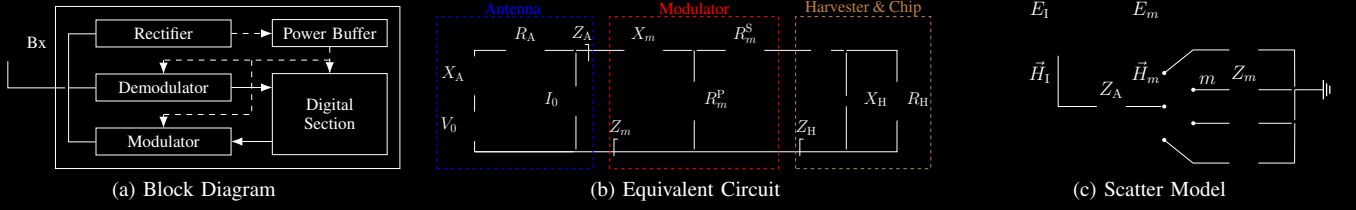(a) Block Diagram   (b) Equivalent Circuit   (c) Scatter Model

Fig. 1. Block diagram, equivalent circuit, and scatter model of a passive backscatter node. The solid and dashed vectors represent signal and energy flows. The backscatter antenna behaves as a constant power source, where the voltage V_0 and current I_0 are introduced by incident electric field $\vec{E}_\mathrm{I}$ and magnetic field $\vec{H}_\mathrm{I}$ [37].

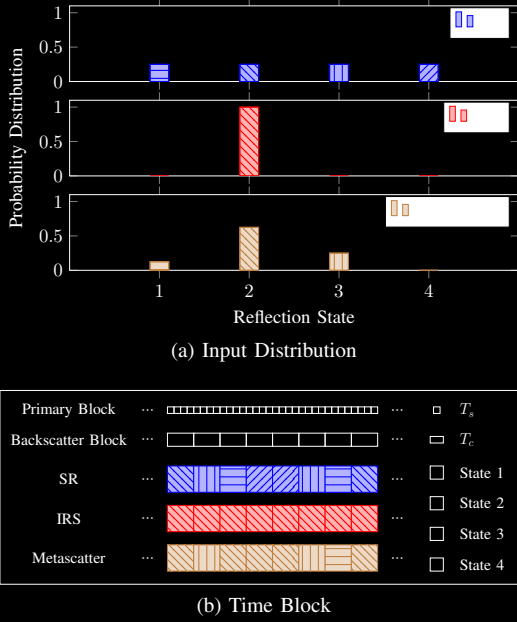(a) Input Distribution

(b) Time Block

Fig. 2. Input probability distribution and time block structure of SR, RIS, and Metascatter. T_s and T_c respectively denote the primary and backscatter symbol period. Within channel coherence time, Metascatter semi-randomly selects reflection state for each backscatter block, with guidance from input probability distribution.
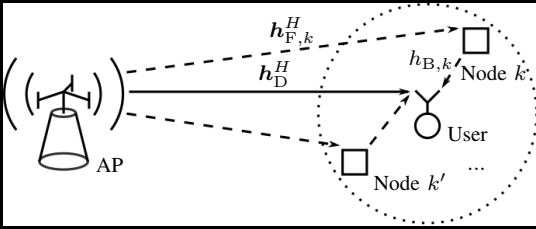

Fig. 3. A Metascatter-enabled single-user multi-node network.

III. METASCATTER-ENABLED NETWORK

A. System Model

As shown in Fig. 3, we propose a Metascatter-enabled single-user multi-node network where two coexisting systems share spectrum, energy and infrastructures. The primary point-to-point transmission from a Q-antenna AP to a single-antenna user is assisted by K nearby single-antenna Metascatters. In the secondary backscatter Multiple Access Channel (MAC) system, the AP serves as the carrier emitter, K nearby single-antenna Metascatters modulate information over reradiated RF signals, and the user decodes their messages. For simplicity, we consider

a quasi-static block fading model where channels remain constant within coherence interval while vary independently between consecutive blocks. Due to physical constraints on load switching, we assume the backscatter symbol period is $N \gg 1$ times longer than primary and consider integer N without loss of generality. We also assume the direct channel and all cascaded channels can be estimated and fed back to the AP.[2] Besides, we omit the signal reflected by two or more times [44] and ignore the time difference of arrival from different paths [9].

Denote the AP-user direct channel as $\boldsymbol{h}_\mathrm{D}^H \in \mathbb{C}^{1 \times Q}$, the AP-node $k \in \mathcal{K} \triangleq \{1,...,K\}$ forward channel as $\boldsymbol{h}_{\mathrm{F},k}^H \in \mathbb{C}^{1 \times Q}$, and the node k-user backward channel as $h_{\mathrm{B},k}$. Also, define the cascaded channel of tag k as $\boldsymbol{h}_{\mathrm{C},k}^H \triangleq h_{\mathrm{B},k} \boldsymbol{h}_{\mathrm{F},k}^H \in \mathbb{C}^{1 \times Q}$, and $\boldsymbol{H}_\mathrm{C} \triangleq [\boldsymbol{h}_{\mathrm{C},1},...,\boldsymbol{h}_{\mathrm{C},K}]^H \in \mathbb{C}^{K \times Q}$. Let $x_\mathcal{K} \triangleq (x_1,...,x_K)$ be the backscatter symbol tuple of all Metascatters. Consider the signal model during one backscatter block (i.e., N primary blocks). Under perfect synchronization, the equivalent primary channel is a function of *coded* backscatter symbols

$$\boldsymbol{h}_\mathrm{E}^H(x_\mathcal{K}) \triangleq \boldsymbol{h}_\mathrm{D}^H + \sum_{k \in \mathcal{K}} \alpha_k \boldsymbol{h}_{\mathrm{C},k}^H x_k \tag{4a}$$

$$= \boldsymbol{h}_\mathrm{D}^H + \boldsymbol{x}^H \mathrm{diag}(\boldsymbol{\alpha}) \boldsymbol{H}_\mathrm{C}, \tag{4b}$$

where α_k is the amplitude reflect ratio of Metascatter k, $\boldsymbol{\alpha} \triangleq [\alpha_1,...,\alpha_K]^T \in \mathbb{R}_+^{K \times 1}$, $x_k \in \mathcal{X} \triangleq \{c_1,...,c_M\}$ is the coded backscatter symbol of Metascatter k, and $\boldsymbol{x} \triangleq [x_1,...,x_K]^H \in \mathbb{C}^{K \times 1}$. The signal received by the user at primary block $n \in \mathcal{N} \triangleq \{1,...,N\}$ is

$$y[n] = \boldsymbol{h}_\mathrm{E}^H(x_\mathcal{K}) \boldsymbol{w} s[n] + v[n], \tag{5}$$

where $s \sim \mathcal{CN}(0,1)$ is the primary symbol, $v \sim \mathcal{CN}(0,\sigma_v^2)$ is the Additive White Gaussian Noise (AWGN), and $\boldsymbol{w} \in \mathbb{C}^{Q \times 1}$ is the active beamforming vector with average power constraint $\|\boldsymbol{w}\|^2 \leq P$.

Remark 2. *Metascatter involves a symbiotic MAC where the primary and backscatter symbols of different duration are mixed by Multiplication Coding (MC) instead of Superposition Coding (SC). For each node, the reflection coefficient not only encodes the backscatter message, but also influences the equivalent primary channel* (4). *To accommodate such signal characteristics, novel receiving strategy apart from SIC is desired to better utilize the reflection pattern and boost the primary-backscatter tradeoff.*

[2]Due to the lack of RF chains at the passive tag, accurate and efficient CSI acquisition at the AP can be challenging. One possibility is the AP sends training pilots, the tags respond in predefined manners, and the user performs least-square estimation with feedbacks [41]–[43].
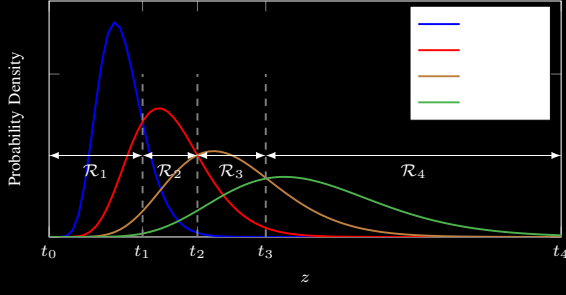
Fig. 4. PDF of total received energy per backscatter block, conditioned on different input hypothesis. Here, the convex ML decision regions are generally rate-suboptimal except for equiprobable inputs.

B. Receiving Strategy

We propose a Metascatter receiver where the backscatter messages of all Metascatters are first jointly and semi-coherently detected using total received energy per backscatter block, then modeled within equivalent channel (4) as dynamic passive beamforming. Compared with ML and SIC, Metascatter receiver allows practical and low-complexity node multiple access with minor adjustment over legacy equipments.

At a specific backscatter block, denote $m_k \in \mathcal{M}$ as the state index of Metascatter k, and let $m_{\mathcal{K}} \triangleq (m_1,...,m_K)$ be the state index tuple of all Metascatters. Conditioned on $m_{\mathcal{K}}$, the received signal at primary block n is subject to the variation of $s[n]$ and $v[n]$, distributed as $y[n] \sim \mathcal{CN}(0, \sigma_{m_{\mathcal{K}}}^2)$ with

$$\sigma_{m_{\mathcal{K}}}^2 = |\boldsymbol{h}_{\mathrm{E}}^H(x_{m_{\mathcal{K}}})\boldsymbol{w}|^2 + \sigma_v^2, \qquad (6)$$

where x_{m_k} and $x_{m_{\mathcal{K}}}$ are the symbol and symbol tuple associated with state m_k and state tuple $m_{\mathcal{K}}$, respectively.[3] Also, denote the total received energy within backscatter block as $z = \sum_{n=1}^{N} |y[n]|^2$. As the sum of N independent and identically distributed (i.i.d.) exponential variables, the Probability Density Function (PDF) of z conditioned on $m_{\mathcal{K}}$ follows Erlang distribution

$$f(z|\mathcal{H}_{m_{\mathcal{K}}}) = \frac{z^{N-1}\exp(-z/\sigma_{m_{\mathcal{K}}}^2)}{\sigma_{m_{\mathcal{K}}}^{2N}(N-1)!}, \qquad (7)$$

where $\mathcal{H}_{m_{\mathcal{K}}}$ denotes hypothesis $m_{\mathcal{K}}$. To accommodate backscatter characteristics and reduce decoding complexity, we consider a joint semi-coherent detection for all Metascatters over accumulated energy z. Once disjoint energy decision regions are determined, we can construct a Discrete Thresholding Multiple Access Channel (DTMAC) and formulate the transition probability from input $x_{m_{\mathcal{K}}}$ to output $\hat{x}_{m'_{\mathcal{K}}}$ as

$$P(\hat{x}_{m'_{\mathcal{K}}}|x_{m_{\mathcal{K}}}) = \int_{\mathcal{R}_{m'_{\mathcal{K}}}} f(z|\mathcal{H}_{m_{\mathcal{K}}})dz, \qquad (8)$$

where $\mathcal{R}_{m'_{\mathcal{K}}}$ is the decision region of hypothesis $\mathcal{H}_{m'_{\mathcal{K}}}$. An example of ML energy decision is illustrated in Fig. 4.

Remark 3. *The rate-optimal thresholding channel design remains under-investigated, and some attempts were made for single source with binary inputs in [45], [46]. For non-binary*

---

[3] x_k and $x_{\mathcal{K}}$ are random variables, while x_{m_k} and $x_{m_{\mathcal{K}}}$ are their instances indexed by m_k and $m_{\mathcal{K}}$.

inputs with general distribution, the optimal decision region for each letter can be non-convex (i.e., with non-adjacent partitions) and the optimal number of thresholds is still unknown.

In the following context, we restrict all decision regions to convex and optimize decision thresholds accordingly. That is, for any bijective mapping $f : m_{\mathcal{K}} \to \mathcal{L} \triangleq \{1,...,M^K\}$, the decision region of letter $l \in \mathcal{L}$ is defined as $\mathcal{R}_l \triangleq [t_{l-1}, t_l)$, where $t_{l-1} \le t_l$. We also define the decision threshold vector as $\boldsymbol{t} \triangleq [t_0,...,t_L]^T \in \mathbb{R}_+^{(L+1)\times 1}$.

C. Achievable Rates

Denote the input probability of state m_k of Metascatter node k as $P_k(x_{m_k})$, and define the input probability distribution vector of node k as $\boldsymbol{p}_k \triangleq [P_k(c_1),...,P_k(c_M)]^T \in \mathbb{R}^{M\times 1}$. With independent encoding at all nodes, the probability of backscatter symbol tuple $x_{m_{\mathcal{K}}}$ is

$$P_{\mathcal{K}}(x_{m_{\mathcal{K}}}) = \prod_{k\in\mathcal{K}} P_k(x_{m_k}). \qquad (9)$$

Similar to [47], we define the backscatter information function between input symbol tuple instance $x_{m_{\mathcal{K}}}$ and output symbol tuple $\hat{x}_{\mathcal{K}}$ as

$$I^{\mathrm{B}}(x_{m_{\mathcal{K}}};\hat{x}_{\mathcal{K}}) \triangleq \sum_{m'_{\mathcal{K}}} P(\hat{x}_{m'_{\mathcal{K}}}|x_{m_{\mathcal{K}}}) \log \frac{P(\hat{x}_{m'_{\mathcal{K}}}|x_{m_{\mathcal{K}}})}{P(\hat{x}_{m'_{\mathcal{K}}})}, \qquad (10)$$

where $P(\hat{x}_{m'_{\mathcal{K}}}) = \sum_{m_{\mathcal{K}}} P_{\mathcal{K}}(x_{m_{\mathcal{K}}})P(\hat{x}_{m'_{\mathcal{K}}}|x_{m_{\mathcal{K}}})$. We also define the backscatter marginal information of letter x_{m_k} of node k as

$$I_k^{\mathrm{B}}(x_{m_k};\hat{x}_{\mathcal{K}}) \triangleq \sum_{m_{\mathcal{K}\backslash\{k\}}} P_{\mathcal{K}\backslash\{k\}}(x_{m_{\mathcal{K}\backslash\{k\}}}) I^{\mathrm{B}}(x_{m_{\mathcal{K}}};\hat{x}_{\mathcal{K}}), \quad (11)$$

where $P_{\mathcal{K}\backslash\{k\}}(x_{m_{\mathcal{K}\backslash\{k\}}}) = \prod_{q\in\mathcal{K}\backslash\{k\}} P_q(x_{m_q})$. Moreover, we can write the backscatter mutual information as

$$I^{\mathrm{B}}(x_{\mathcal{K}};\hat{x}_{\mathcal{K}}) = \sum_{m_{\mathcal{K}}} P_{\mathcal{K}}(x_{m_{\mathcal{K}}}) I^{\mathrm{B}}(x_{m_{\mathcal{K}}};\hat{x}_{\mathcal{K}}). \qquad (12)$$

Once backscatter messages are successfully decoded, we can re-encode to determine $x_{\mathcal{K}}$ and retrieve equivalent primary channel by (4). We define the primary information function conditioned on backscatter symbol tuple $x_{m_{\mathcal{K}}}$ as

$$I^{\mathrm{P}}(s;y|x_{m_{\mathcal{K}}}) \triangleq \log\left(1 + \frac{|\boldsymbol{h}_{\mathrm{E}}^H(x_{m_{\mathcal{K}}})\boldsymbol{w}|^2}{\sigma_v^2}\right), \qquad (13)$$

the primary marginal information conditioned on letter x_{m_k} of node k as

$$I_k^{\mathrm{P}}(s;y|x_{m_k}) \triangleq \sum_{m_{\mathcal{K}\backslash\{k\}}} P_{\mathcal{K}\backslash\{k\}}(x_{m_{\mathcal{K}\backslash\{k\}}}) I^{\mathrm{P}}(s;y|x_{m_{\mathcal{K}}}), \quad (14)$$

and the primary ergodic mutual information as

$$I^{\mathrm{P}}(s;y|x_{\mathcal{K}}) = \sum_{m_{\mathcal{K}}} P_{\mathcal{K}}(x_{m_{\mathcal{K}}}) I^{\mathrm{P}}(s;y|x_{m_{\mathcal{K}}}). \qquad (15)$$

Finally, with a slight abuse of notation, we define the corresponding weighted sum information function, marginal information, and mutual information respectively as

$$I(x_{m_{\mathcal{K}}}) \triangleq \rho I^{\mathrm{P}}(s;y|x_{m_{\mathcal{K}}}) + (1-\rho)I^{\mathrm{B}}(x_{m_{\mathcal{K}}};\hat{x}_{\mathcal{K}}), \qquad (16)$$

$$I_k(x_{m_k}) \triangleq \rho I_k^{\mathrm{P}}(s;y|x_{m_k}) + (1-\rho)I_k^{\mathrm{B}}(x_{m_k};\hat{x}_{\mathcal{K}}), \qquad (17)$$

$$I(x_{\mathcal{K}}) \triangleq \rho I^{\mathrm{P}}(s;y|x_{\mathcal{K}}) + (1-\rho)I^{\mathrm{B}}(x_{\mathcal{K}};\hat{x}_{\mathcal{K}}), \qquad (18)$$

where $0\leq\rho\leq1$ is the relative priority of the primary link.

IV. INPUT DISTRIBUTION, ACTIVE BEAMFORMING, AND DECISION THRESHOLD DESIGN

To characterize the achievable primary-(total-)backscatter rate region of the proposed Metascatter-enabled network, we aim to maximize the weighted sum mutual information with respect to node input distributions $\{\boldsymbol{p}_k\}_{k\in\mathcal{K}}$, active beamforming vector $\boldsymbol{w}$, and decision threshold vector $\boldsymbol{t}$ as

$$\max_{\{\boldsymbol{p}_k\}_{k\in\mathcal{K}},\boldsymbol{w},\boldsymbol{t}\in\mathbb{R}_+^{L+1}} \quad I(x_{\mathcal{K}}) \tag{19a}$$

$$\text{s.t.} \quad \sum_{m_k} P_k(x_{m_k})=1, \quad \forall k, \tag{19b}$$

$$P_k(x_{m_k})\geq0, \quad \forall k,m_k, \tag{19c}$$

$$\|\boldsymbol{w}\|^2\leq P, \tag{19d}$$

$$t_{l-1}\leq t_l, \quad \forall l. \tag{19e}$$

Problem (19) is highly non-convex, and we propose a BCD algorithm that iteratively updates $\{\boldsymbol{p}_k\}_{k\in\mathcal{K}}$, $\boldsymbol{w}$ and $\boldsymbol{t}$ until convergence.

A. Input Distribution

For any given $\boldsymbol{w}$ and $\boldsymbol{t}$, we can construct the equivalent DTMAC by (8) and simplify (19) to

$$\max_{\{\boldsymbol{p}_k\}_{k\in\mathcal{K}}} \quad I(x_{\mathcal{K}}) \tag{20a}$$

$$\text{s.t.} \quad (19b),(19c), \tag{20b}$$

which involves coupled term $\prod_{k\in\mathcal{K}}P_k(x_{m_k})$ and is non-convex when $K>1$. Next, we propose a numerical method that evaluate the KKT input distribution by limit of sequences.

Remark 4. *As pointed out in [48], KKT conditions are generally necessary but insufficient for total rate maximization in discrete memoryless MAC. Therefore, KKT solutions may end up being saddle points of problem (20).*

Following [47], we first recast KKT conditions to their equivalent form for problem (20), then propose an iterative method that guarantees input distribution satisfying above conditions on convergence.

Proposition 1. *The KKT optimality conditions for problem (20) are equivalent to, $\forall k,m_k$,*

$$I_k^{\star}(x_{m_k})=I^{\star}(x_{\mathcal{K}}), \quad P_k^{\star}(x_{m_k})>0, \tag{21a}$$

$$I_k^{\star}(x_{m_k})\leq I^{\star}(x_{\mathcal{K}}), \quad P_k^{\star}(x_{m_k})=0. \tag{21b}$$

Proof. Please refer to Appendix A. □

For each node, (21a) suggests each probable state should produce the same marginal information (averaged over all states of other nodes), while (21b) implies any state with potentially less marginal information should not be used.

Proposition 2. *The KKT input probability of node k of state m_k is given by the converging point of the sequence*

$$P_k^{(r+1)}(x_{m_k})=\frac{P_k^{(r)}(x_{m_k})\exp\left(\frac{\rho}{1-\rho}I_k^{(r)}(x_{m_k})\right)}{\sum_{m_k'}P_k^{(r)}(x_{m_k'})\exp\left(\frac{\rho}{1-\rho}I_k^{(r)}(x_{m_k'})\right)}, \tag{22}$$

Algorithm 1: Numerical Evaluation of KKT Input Distribution

Input: K, N, $\boldsymbol{h}_{\mathrm{D}}^H$, $\boldsymbol{H}_{\mathrm{C}}$, $\boldsymbol{\alpha}$, $\mathcal{X}$, σ_v^2, ρ, $\boldsymbol{w}$, $\boldsymbol{t}$, ϵ
Output: $\{\boldsymbol{p}_k^{\star}\}_{k\in\mathcal{K}}$
1: Set $\boldsymbol{h}_{\mathrm{E}}^H(x_{m_{\mathcal{K}}})$, $\forall m_{\mathcal{K}}$ by (4)
2:   $\sigma_{m_{\mathcal{K}}}^2$, $\forall m_{\mathcal{K}}$ by (6)
3:   $f(z|\mathcal{H}_{m_{\mathcal{K}}})$, $\forall m_{\mathcal{K}}$ by (7)
4:   $P(\hat{x}_{m_{\mathcal{K}}'}|x_{m_{\mathcal{K}}})$, $\forall m_{\mathcal{K}},m_{\mathcal{K}}'$ by (8)
5: Initialize $r\leftarrow0$
6:   $\boldsymbol{p}_k^{(0)}>\boldsymbol{0}$, $\forall k$
7: Get $P_{\mathcal{K}}^{(r)}(x_{m_{\mathcal{K}}})$, $\forall m_{\mathcal{K}}$ by (9)
8:   $I^{(r)}(x_{m_{\mathcal{K}}})$, $\forall m_{\mathcal{K}}$ by (10), (13), (16)
9:   $I_k^{(r)}(x_{m_k})$, $\forall k,m_k$ by (11), (14), (17)
10:   $I^{(r)}(x_{\mathcal{K}})$ by (12), (15), (18)
11: **Repeat**
12:   Update $r\leftarrow r+1$
13:     $\boldsymbol{p}_k^{(r)}$, $\forall k$ by (22)
14:   Redo step 7–10
15: **Until** $I^{(r)}(x_{\mathcal{K}})-I^{(r-1)}(x_{\mathcal{K}})\leq\epsilon$

---

where r is the iteration index and $\boldsymbol{p}_k^{(0)}>\boldsymbol{0}$, $\forall k$.

Proof. Please refer to Appendix B. □

At each iteration, the input distribution of node k is evaluated over updated input distribution of node 1 to $k-1$, together with previous input distribution of node $k+1$ to K. The KKT input distribution design is summarized in Algorithm 1.

B. Active Beamforming

For any given $\{\boldsymbol{p}_k\}_{k\in\mathcal{K}}$ and $\boldsymbol{t}$, problem (19) reduces to

$$\max_{\boldsymbol{w}} \quad I(x_{\mathcal{K}}) \tag{23a}$$

$$\text{s.t.} \quad (19d), \tag{23b}$$

which is still non-convex due to integration and entropy terms. To see this, we explicitly write (23a) as (24) at the bottom of page 6, where

$$Q\left(N,\frac{t_{l-1}}{\sigma_{m_{\mathcal{K}}}^2},\frac{t_l}{\sigma_{m_{\mathcal{K}}}^2}\right)=\frac{\int_{t_{l-1}/\sigma_{m_{\mathcal{K}}}^2}^{t_l/\sigma_{m_{\mathcal{K}}}^2}z^{N-1}\exp(-z)dz}{(N-1)!} \tag{25}$$

is the regularized incomplete Gamma function that substitutes the DTMAC transition probability (8). Its series representation is given by [49, Theorem 3]

$$Q\left(N,\frac{t_{l-1}}{\sigma_{m_{\mathcal{K}}}^2},\frac{t_l}{\sigma_{m_{\mathcal{K}}}^2}\right)=\exp\left(-\frac{t_{l-1}}{\sigma_{m_{\mathcal{K}}}^2}\right)\sum_{n=0}^{N-1}\frac{\left(\frac{t_{l-1}}{\sigma_{m_{\mathcal{K}}}^2}\right)^n}{n!}$$

$$-\exp\left(-\frac{t_l}{\sigma_{m_{\mathcal{K}}}^2}\right)\sum_{n=0}^{N-1}\frac{\left(\frac{t_l}{\sigma_{m_{\mathcal{K}}}^2}\right)^n}{n!}. \tag{26}$$

Next, we derive the gradients of (26) and (24) w.r.t. $\boldsymbol{w}^*$ as (27) and (28) at the end of page 7 and 7, respectively. It allows problem (23) to be solved by the PGD method, where any unregulated beamforming vector $\bar{\boldsymbol{w}}$ can be projected onto the feasible domain of average transmit power constraint (19d) by

$$\boldsymbol{w}=\sqrt{P}\frac{\bar{\boldsymbol{w}}}{\max\left(\sqrt{P},\|\bar{\boldsymbol{w}}\|\right)}. \tag{29}$$

We present the iterative active beamforming design accelerated by backtracking line search in Algorithm 2.

C. Decision Threshold

For any given $\{\boldsymbol{p}_k\}_{k\in\mathcal{K}}$ and $\boldsymbol{w}$, problem (19) reduces to

$$\max_{\boldsymbol{t}\in\mathbb{R}_+^{L+1}} \quad I(x_{\mathcal{K}}) \tag{30a}$$

$$\text{s.t.} \quad (19e), \tag{30b}$$

where it is trivial to conclude $t_0^\star = 0$ and $t_L^\star = \infty$ for energy-based backscatter detection.

Remark 5. *Backscatter detection (and decision design) has no impact on primary achievable rate. When nodes transmit at non-zero total rate, the user can re-encode backscatter messages to recover coded backscatter tuple $x_{\mathcal{K}}$ at each block. Otherwise, $x_{\mathcal{K}}$ can be fully deterministic and known to the user.*

Remark 5 suggests any $\boldsymbol{t}$ maximizes total backscatter mutual information $I^{\mathrm{B}}(x_{\mathcal{K}};\hat{x}_{\mathcal{K}})$ is also optimal for problem (30).

Remark 6. *In terms of total backscatter rate, the nodes can be regarded as an equivalent source with augmented alphabet of symbol tuple $x_{m_{\mathcal{K}}}$, and the DTMAC (8) essentially reduces to a Discrete Memoryless Thresholding Channel (DMTC).*

Finally, we can employ existing thresholding design for DMTC to solve problem (30). For example, [50] first discretized the continuous energy z into numerous output bins, then grouped adjacent bins to maximize mutual

---

Algorithm 2: Iterative Active Beamforming Design by PGD with Backtracking Line Search

Input: $Q, N, \boldsymbol{h}_{\mathrm{D}}^H, \boldsymbol{H}_{\mathrm{C}}, \boldsymbol{\alpha}, \mathcal{X}, P, \sigma_v^2, \rho, \{\boldsymbol{p}_k\}_{k\in\mathcal{K}}, \boldsymbol{t}, \alpha, \beta, \gamma, \epsilon$
Output: $\boldsymbol{w}^\star$

1: Set $\boldsymbol{h}_{\mathrm{E}}^H(x_{m_{\mathcal{K}}})$, $\forall m_{\mathcal{K}}$ by (4)
2: $\quad P_{\mathcal{K}}(x_{m_{\mathcal{K}}})$, $\forall m_{\mathcal{K}}$ by (9)
3: Initialize $r \leftarrow 0$
4: $\quad \boldsymbol{w}^{(0)}, \|\boldsymbol{w}^{(0)}\|^2 \leq P$
5: Get $(\sigma_{m_{\mathcal{K}}}^{(r)})^2$, $\forall m_{\mathcal{K}}$ by (6)
6: $\quad Q^{(r)}\big(N, \frac{t_{l-1}}{\sigma_{m_{\mathcal{K}}}^2}, \frac{t_l}{\sigma_{m_{\mathcal{K}}}^2}\big)$, $\forall m_{\mathcal{K}}, l$ by (25) or (26)
7: $\quad I^{(r)}(x_{\mathcal{K}})$ by (24)
8: $\quad \nabla_{\boldsymbol{w}^*} Q^{(r)}\big(N, \frac{t_{l-1}}{\sigma_{m_{\mathcal{K}}}^2}, \frac{t_l}{\sigma_{m_{\mathcal{K}}}^2}\big)$, $\forall m_{\mathcal{K}}, l$ by (27)
9: $\quad \nabla_{\boldsymbol{w}^*} I^{(r)}(x_{\mathcal{K}})$ by (28)
10: **Repeat**
11: $\quad$ Update $r \leftarrow r+1$
12: $\quad\quad \gamma^{(r)} \leftarrow \gamma$
13: $\quad\quad \bar{\boldsymbol{w}}^{(r)} \leftarrow \boldsymbol{w}^{(r-1)} + \gamma \nabla_{\boldsymbol{w}^*} I^{(r-1)}(x_{\mathcal{K}})$
14: $\quad\quad \boldsymbol{w}^{(r)}$ by (29)
15: $\quad$ Redo step 5–7
16: $\quad$ **While** $\quad I^{(r)}(x_{\mathcal{K}}) \quad < \quad I^{(r-1)}(x_{\mathcal{K}}) \quad +$
$\alpha\gamma\|\nabla_{\boldsymbol{w}^*} I^{(r-1)}(x_{\mathcal{K}})\|^2$
17: $\quad\quad$ Set $\gamma^{(r)} \leftarrow \beta\gamma^{(r)}$
18: $\quad\quad$ Redo step 13–15
19: $\quad$ **End While**
20: $\quad$ Redo step 8, 9
21: **Until** $\|\boldsymbol{w}^{(r)} - \boldsymbol{w}^{(r-1)}\| \leq \epsilon$

$$I(x_{\mathcal{K}}) = \sum_{m_{\mathcal{K}}} P_{\mathcal{K}}(x_{m_{\mathcal{K}}}) \Bigg(\rho\log\Big(1 + \frac{|\boldsymbol{h}_{\mathrm{E}}^H(x_{m_{\mathcal{K}}})\boldsymbol{w}|^2}{\sigma_v^2}\Big) + (1-\rho)\sum_l Q\Big(N, \frac{t_{l-1}}{\sigma_{m_{\mathcal{K}}}^2}, \frac{t_l}{\sigma_{m_{\mathcal{K}}}^2}\Big)\log\frac{Q\Big(N, \frac{t_{l-1}}{\sigma_{m_{\mathcal{K}}}^2}, \frac{t_l}{\sigma_{m_{\mathcal{K}}}^2}\Big)}{\sum_{m_{\mathcal{K}}'} P_{\mathcal{K}}(x_{m_{\mathcal{K}}'}) Q\Big(N, \frac{t_{l-1}}{\sigma_{m_{\mathcal{K}}'}^2}, \frac{t_l}{\sigma_{m_{\mathcal{K}}'}^2}\Big)} \Bigg) \tag{24}$$

$$\nabla_{\boldsymbol{w}^*} Q\Big(N, \frac{t_{l-1}}{\sigma_{m_{\mathcal{K}}}^2}, \frac{t_l}{\sigma_{m_{\mathcal{K}}}^2}\Big) = \frac{\boldsymbol{h}_{\mathrm{E}}(x_{m_{\mathcal{K}}})\boldsymbol{h}_{\mathrm{E}}^H(x_{m_{\mathcal{K}}})\boldsymbol{w}}{\big(|\boldsymbol{h}_{\mathrm{E}}^H(x_{m_{\mathcal{K}}})\boldsymbol{w}|^2 + \sigma_v^2\big)^2}$$
$$\times \Bigg(t_l \exp\Big(-\frac{t_l}{|\boldsymbol{h}_{\mathrm{E}}^H(x_{m_{\mathcal{K}}})\boldsymbol{w}|^2 + \sigma_v^2}\Big)\Big(-1 + \sum_{n=1}^{N-1} \frac{n\Big(\frac{t_l}{|\boldsymbol{h}_{\mathrm{E}}^H(x_{m_{\mathcal{K}}})\boldsymbol{w}|^2 + \sigma_v^2}\Big)^{n-1} - \Big(\frac{t_l}{|\boldsymbol{h}_{\mathrm{E}}^H(x_{m_{\mathcal{K}}})\boldsymbol{w}|^2 + \sigma_v^2}\Big)^n}{n!}\Big)$$
$$- t_{l-1} \exp\Big(-\frac{t_{l-1}}{|\boldsymbol{h}_{\mathrm{E}}^H(x_{m_{\mathcal{K}}})\boldsymbol{w}|^2 + \sigma_v^2}\Big)\Big(-1 + \sum_{n=1}^{N-1} \frac{n\Big(\frac{t_{l-1}}{|\boldsymbol{h}_{\mathrm{E}}^H(x_{m_{\mathcal{K}}})\boldsymbol{w}|^2 + \sigma_v^2}\Big)^{n-1} - \Big(\frac{t_{l-1}}{|\boldsymbol{h}_{\mathrm{E}}^H(x_{m_{\mathcal{K}}})\boldsymbol{w}|^2 + \sigma_v^2}\Big)^n}{n!}\Big)\Bigg) \tag{27}$$

$$\nabla_{\boldsymbol{w}^*} I(x_{\mathcal{K}}) = \sum_{m_{\mathcal{K}}} P_{\mathcal{K}}(x_{m_{\mathcal{K}}}) \Bigg(\rho\frac{\boldsymbol{h}_{\mathrm{E}}(x_{m_{\mathcal{K}}})\boldsymbol{h}_{\mathrm{E}}^H(x_{m_{\mathcal{K}}})\boldsymbol{w}}{|\boldsymbol{h}_{\mathrm{E}}^H(x_{m_{\mathcal{K}}})\boldsymbol{w}|^2 + \sigma_v^2} + (1-\rho)\sum_l \Big(\log\frac{Q\Big(N, \frac{t_{l-1}}{\sigma_{m_{\mathcal{K}}}^2}, \frac{t_l}{\sigma_{m_{\mathcal{K}}}^2}\Big)}{\sum_{m_{\mathcal{K}}'} P_{\mathcal{K}}(x_{m_{\mathcal{K}}'}) Q\Big(N, \frac{t_{l-1}}{\sigma_{m_{\mathcal{K}}'}^2}, \frac{t_l}{\sigma_{m_{\mathcal{K}}'}^2}\Big)} + 1\Big)$$
$$\times \nabla_{\boldsymbol{w}^*} Q\Big(N, \frac{t_{l-1}}{\sigma_{m_{\mathcal{K}}}^2}, \frac{t_l}{\sigma_{m_{\mathcal{K}}}^2}\Big) - \frac{Q\Big(N, \frac{t_{l-1}}{\sigma_{m_{\mathcal{K}}}^2}, \frac{t_l}{\sigma_{m_{\mathcal{K}}}^2}\Big)\sum_{m_{\mathcal{K}}'} P_{\mathcal{K}}(x_{m_{\mathcal{K}}'}) \nabla_{\boldsymbol{w}^*} Q\Big(N, \frac{t_{l-1}}{\sigma_{m_{\mathcal{K}}'}^2}, \frac{t_l}{\sigma_{m_{\mathcal{K}}'}^2}\Big)}{\sum_{m_{\mathcal{K}}'} P_{\mathcal{K}}(x_{m_{\mathcal{K}}'}) Q\Big(N, \frac{t_{l-1}}{\sigma_{m_{\mathcal{K}}'}^2}, \frac{t_l}{\sigma_{m_{\mathcal{K}}'}^2}\Big)} \Bigg) \tag{28}$$
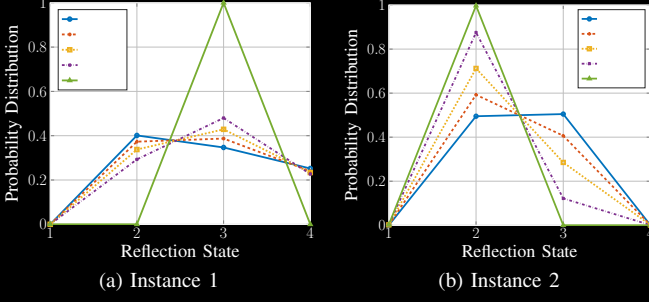
Fig. 5. Typical input distributions vs. weight ρ for a Metascatter with $M=4$ inputs.

Fig. 6. Average primary-(total-)backscatter rate regions for different input distribution and decision threshold schemes.

information using Dynamic Programming (DP) accelerated by Shor-Moran-Aggarwal-Wilber-Klawe (SMAWK) algorithm. In [51], the authors first proved the optimality condition for any three neighbor thresholds, then fix t_0, traverse t_1, and sequentially optimizes the others by bisection. Both will be compared with ML decision [52]

$$t_l^{\mathrm{ML}} = N \frac{\sigma_{l-1}^2 \sigma_l^2}{\sigma_{l-1}^2 - \sigma_l^2} \log \frac{\sigma_{l-1}^2}{\sigma_l^2}, \quad l \in \mathcal{L} \setminus \{0, L\}, \qquad (31)$$

which is generally suboptimal for problem (30) except for equiprobable inputs at all nodes.

V. SIMULATION RESULTS

In this section, we provide numerical results to evaluate the proposed input, beamforming and decision design over a single-user multi-node Metascatter-enabled network. We assume the distance between AP and user is $10\,\mathrm{m}$, and $K=2$ Metascatters are uniformly dropped within a disk centered at the user of radius $1\,\mathrm{m}$. The carrier frequency is $f=200\mathrm{MHz}$, and we consider i.i.d. Ricean fading between all terminals. For direct, forward and backward links, we set the path loss exponents to 2.6, 2.4 and 2, and the Ricean factor to 5, 5 and 10, respectively. The AP has $Q=4$ antennas with maximum average transmit power $P=36\mathrm{dBm}$. All nodes have amplitude reflect ratio $\alpha=0.5$, symbol period ratio $N=20$, and perform QAM with $M=2$ input states. The user is with average noise power $\sigma_v^2=70\mathrm{dBm}$ and receive antenna gain $3\,\mathrm{dBi}$. All rate regions are averaged over at least 1000 instances, where "PSP" and "BSP" means primary and backscatter symbol periods, respectively. We choose decision design by SMAWK [50] as reference, and select discretize boundaries uniformly over the $95\,\%$ confidence region of edge hypotheses. The parameters remain fixed unless otherwise specified.

A. Input Distribution vs. Weight

In Fig. 5, we present typical input distributions of a single Metascatter with $M=4$ inputs under different weight ρ. Fig. 5(a) and 5(b) are obtained from i.i.d. drop and channel realizations. We note that even for $\rho=0$ (i.e., best backscatter performance), the optimal input distribution is not equiprobable like SR, and adaptive channel coding can further increase total backscatter rate based on CSI. On the other hand, the optimal input distribution becomes fully deterministic at $\rho=1$ (i.e., best
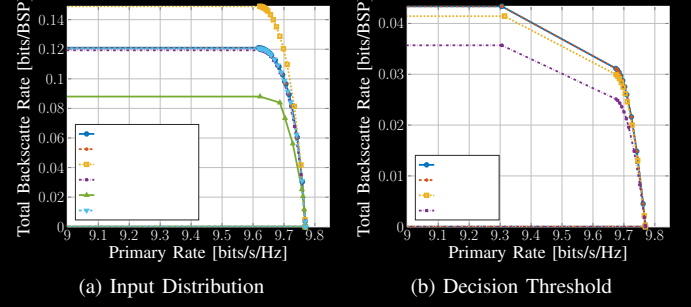
primary performance), where the state maximizes equivalent primary channel (4) strength is chosen with probability 1. In this case, Metascatter boils down to a RIS element with M discrete states. As ρ moves from 0 to 1, the optimal input distribution becomes gradually biased to one state and flexibly balances the primary-backscatter tradeoff.

B. Rate Region vs. Input, Beamforming, and Decision Schemes

Fig. 6(a) compares the achievable rate regions by following input designs.

- **Exhaustion:** K-dimensional grid search over probability simplex;
- **KKT:** results of Algorithm 1;
- **Cooperation:** backscatter cooperation/joint encoding at all Metascatters, tuple input distribution/joint probability array optimization by Blahut-Arimoto algorithm [53], [54];
- **Marginalization:** marginal distributions of joint probability array;
- **Decomposition:** normalized tensors of rank-1 Canonical Polyadic (CP) decomposition of joint probability array;
- **Randomization:** Gaussian recovery from joint probability array [55].

We notice adaptive joint encoding at all Metascatters provides the outer bound of rate region. However, it involves arbitrarily dependent codewords, and backscatter cooperation between passive nodes is generally unaffordable. In contrast, the rate region of KKT input design in Algorithm 1 approaches that of exhaustive search, and the loss is negligible for $K=2$. Although the randomization method [55] returns similar rate region, it requires solving $K+1$ linear programming problems before applying Gaussian recovery. The marginal distribution is slightly worse than KKT despite having the same computational complexity, while the approximation from CP decomposition is unsatisfying.

Fig. 6(b) compares the achievable rate region by following threshold schemes.

- **DP:** sequential quantizer grouping by dynamic programming [50];
- **SMAWK:** above accelerated by SMAWK algorithm;
- **Bisection:** sequential bisection threshold design [51];
- **ML:** maximum likelihood decision (31) [52].

We observe that input-adaptive threshold designs achieve higher total backscatter rate than ML. This is because the
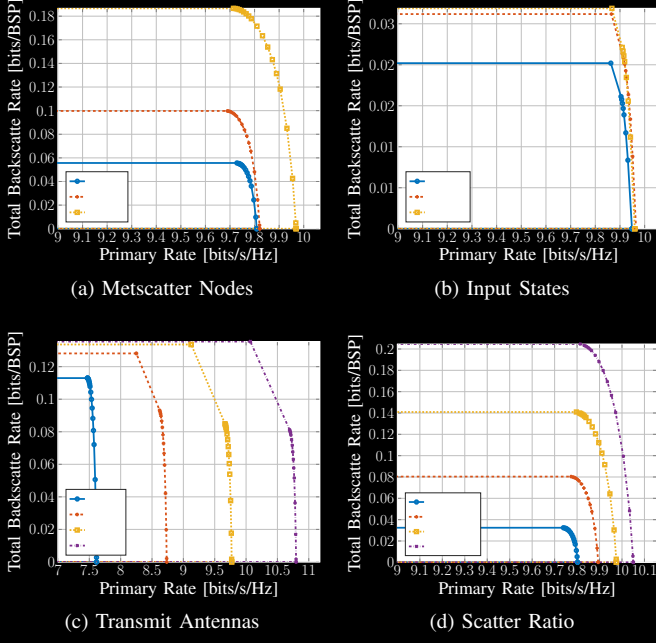
(a) Metscatter Nodes   (b) Input States

(c) Transmit Antennas   (d) Scatter Ratio

Fig. 7. Average primary-(total-)backscatter rate regions.

(a) Node Coverage   (b) Symbol Period Ratio

(c) Carrier Frequency   (d) Average Noise Power

Fig. 8. Average primary-(total-)backscatter rate regions.

decision regions can be flexibly adjusted to enhance the capacity of DTMAC (8). For example, the tuples with negligible input probability should have narrower decision regions than those frequently employed, in order to improve detection performance. It emphasizes the importance of joint input distribution and decision region design.

C. Rate Region vs. System Configuration

We present in 7 the impact of Metascatter nodes, input states, transmit antennas and scatter ratio on the achievable rate region. For the specified scenario, Fig. 7(a) shows the total backscatter rate almost scales proportionally with the number of Metascatter nodes, and the decrease of individual backscatter rate is unobvious. Besides, we conclude from 7(b) that increasing the reflection states has a marginal effect on both primary and backscatter rates. Those two facts motivates the use of numerous elementary/uncomplicated backscatter nodes, instead of high-order transponders or programmable high-resolution surfaces. Figs. 7(c) and 7(d) also prove increasing transmit antennas or scatter ratio can improve both primary and backscatter performance.

Fig. 8(a) shows the tradeoff between coverage disk radius r and achievable rate region. When nodes are far from the user, both primary and backscatter rates decrease due to the product pass loss of forward and backward channels. Under the assumption of ideal backscatter decoding and re-encoding, Fig. 8(b) suggests using lower symbol period ratio N can boost total backscatter rate per primary symbol. However, it requires more frequent detection and re-encoding at the user to maintain the primary rate. When N becomes sufficiently large, total backscatter rate approaches 0 and Metascatters boil down to conventional RIS elements with fixed reflection patterns during whole channel block. In Fig. 8(c), we observe that passive Metascatter achieves higher backscatter rate at lower carrier
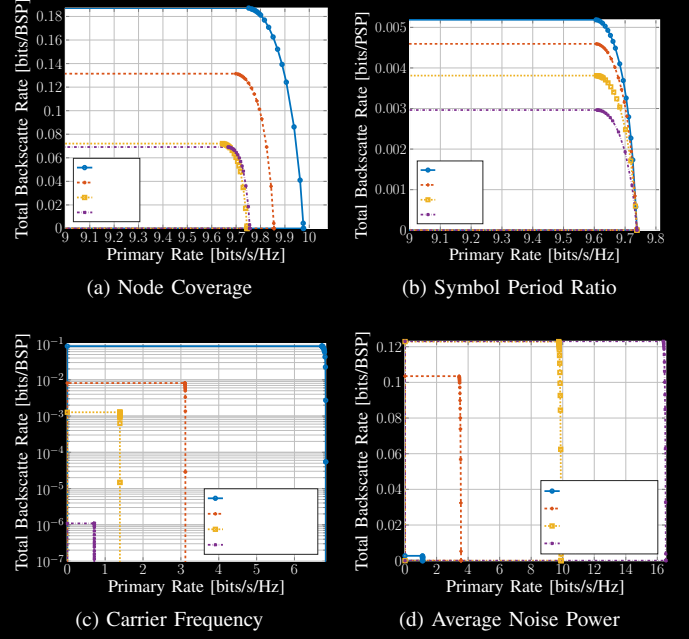
frequency because of preferable propagation loss. Finally, 8(d) prove the performance of energy detection is robust for a wide range of noise power.

VI. CONCLUSION

This paper introduced Metascatter that adapts input distribution of passive backscatter nodes to simultaneously transmit and assist over existing wireless systems. Starting from backscatter principles, we showed how Metascatters bridges and generalizes parasitic source of SR and reflecting element of RIS via smart input design. An application scenario was considered where multiple Metascatters ride over a point-to-point transmission to simultaneously encode self message and perform passive beamforming. To characterize achievable primary-backscatter rate region, we proposed a BCD algorithm that evaluates KKT input distribution in closed form, optimizes active beamforming by PGD, and refines decision regions by existing methods. Numerical results demonstrated the advantage of adaptive node input distribution design for both primary and backscatter subsystems.

One particular interesting question is how to design Metascatters in a multi-user system. If one node can contribute to and be decoded by multiple users, its input distribution may be further adjusted to mimic multi-beam gain of dynamic beamforming [36].

APPENDIX

A. Proof of Proposition 1

Denote the Lagrange multipliers associated with (19b) and (19c) as $\{\nu_k\}_{k\in\mathcal{K}}$ and $\{\lambda_{k,m_k}\}_{k\in\mathcal{K},m_k\in\mathcal{M}}$, respectively. The

Lagrangian function of problem (20) is

$$L = -I(x_\mathcal{K}) + \sum_k \nu_k \left(\sum_{m_k \in \mathcal{M}} P_k(x_{m_k}) - 1 \right)$$
$$- \sum_k \sum_{m_k} \lambda_{k,m_k} P_k(x_{m_k}), \tag{32}$$

and the KKT conditions are, $\forall k, m_k$,

$$-\nabla_{P_k^\star(x_{m_k})} I^\star(x_\mathcal{K}) + \nu_k^\star - \lambda_{k,m_k}^\star = 0, \tag{33a}$$

$$\lambda_{k,m_k}^\star = 0, \quad P_k^\star(x_{m_k}) > 0, \tag{33b}$$

$$\lambda_{k,m_k}^\star \geq 0, \quad P_k^\star(x_{m_k}) = 0. \tag{33c}$$

The directional derivative can be explicitly expressed as

$$\nabla_{P_k^\star(x_{m_k})} I^\star(x_\mathcal{K}) = I_k^\star(x_{m_k}) - (1-\rho). \tag{34}$$

Combining (33) and (34), we have

$$I_k^\star(x_{m_k}) = \nu_k^\star + (1-\rho), \quad P_k^\star(x_{m_k}) > 0, \tag{35a}$$
$$I_k^\star(x_{m_k}) \leq \nu_k^\star + (1-\rho), \quad P_k^\star(x_{m_k}) = 0, \tag{35b}$$

which suggests

$$\sum_{m_k} P_k^\star(x_{m_k}) I_k^\star(x_{m_k}) = \nu_k^\star + (1-\rho). \tag{36}$$

On the other hand, by definition of weighted sum marginal information (17),

$$\sum_{m_k} P_k^\star(x_{m_k}) I_k^\star(x_{m_k}) = I^\star(x_\mathcal{K}), \tag{37}$$

where the right-hand side is irrelevant to k. (35), (36), and (37) together complete the proof.

B. Proof of Proposition 2

We first prove sequence (22) is non-decreasing in weighted sum mutual information. Let $P_\mathcal{K}(x_{m_\mathcal{K}}) = \prod_{q \in \mathcal{K}} P_q(x_{m_q})$ and $P'_\mathcal{K}(x_{m_\mathcal{K}}) = P'_k(x_{m_k}) \prod_{q \in \mathcal{K} \setminus \{k\}} P_q(x_{m_q})$ be two probability distributions with potentially different marginal for tag $k \in \mathcal{K}$ at state $m_k \in \mathcal{M}$, and define an intermediate function $J(P_\mathcal{K}(x_{m_\mathcal{K}}), P'_\mathcal{K}(x_{m_\mathcal{K}}))$ as (38) at the end of page 10. It is straightforward to verify $J(P_\mathcal{K}(x_{m_\mathcal{K}}), P_\mathcal{K}(x_{m_\mathcal{K}})) = I(x_\mathcal{K})$ and $J(P_\mathcal{K}(x_{m_\mathcal{K}}), P'_\mathcal{K}(x_{m_\mathcal{K}}))$ is a concave function for a fixed $P'_\mathcal{K}(x_{m_\mathcal{K}})$. By choosing $\nabla_{P_k^\star(x_{m_k})} J(P_\mathcal{K}(x_{m_\mathcal{K}}), P'_\mathcal{K}(x_{m_\mathcal{K}})) = 0$, we have

$$S'_k(x_{m_k}) - S'_k(x_{i_k}) + (1-\rho) \log \frac{P_k(x_{i_k})}{P_k^\star(x_{m_k})} = 0, \tag{39}$$

where $i_k \neq m_k$ is the reference state and

$$S'_k(x_{m_k}) \triangleq I'_k(x_{m_k}) + (1-\rho) \sum_{m_{\mathcal{K} \setminus \{k\}}} P_{\mathcal{K} \setminus \{k\}}(x_{m_{\mathcal{K} \setminus \{k\}}})$$
$$\times \sum_{m'_\mathcal{K}} P(\hat{x}_{m'_\mathcal{K}} | x_{m_\mathcal{K}}) \log P'_\mathcal{K}(x_{m_\mathcal{K}}). \tag{40}$$

Evidently, $\forall m_k \neq i_k$, (39) boils down to

$$P_k^\star(x_{m_k}) = \frac{P'_k(x_{m_k}) \exp\left(\frac{\rho}{1-\rho} I'_k(x_{m_k}) \right)}{\sum_{m'_k} P'_k(x_{m'_k}) \exp\left(\frac{\rho}{1-\rho} I'_k(x_{m'_k}) \right)}. \tag{41}$$

We also notice $P_k(x_{i_k}) = 1 - \sum_{m_k \neq i_k} P_k^\star(x_{m_k})$ has exactly the same expression as (41). Therefore, the result is irrelevant to the choice of reference state, and (41) is indeed optimal $\forall m_k \in \mathcal{M}$. That is, for a fixed $P'_\mathcal{K}(x_{m_\mathcal{K}})$, choosing $P_k(x_{m_k})$ by (41) ensures

$$J(P_\mathcal{K}(x_{m_\mathcal{K}}), P'_\mathcal{K}(x_{m_\mathcal{K}})) \geq I'(x_\mathcal{K}). \tag{42}$$

On the other hand, it also guarantees

$$\Delta \triangleq I(x_\mathcal{K}) - J(P_\mathcal{K}(x_{m_\mathcal{K}}), P'_\mathcal{K}(x_{m_\mathcal{K}})) \tag{43a}$$

$$= (1-\rho) \sum_{m_k} \frac{P'_k(x_{m_k}) f'_k(x_{m_k})}{\sum_{m'_k} P'_k(x_{m'_k}) f'_k(x_{m'_k})} \sum_{m''_\mathcal{K}} P(\hat{x}_{m''_\mathcal{K}} | x_{m_k})$$
$$\times \log \frac{\sum_{m'_k} P'_k(x_{m'_k}) P(\hat{x}_{m''_\mathcal{K}} | x_{m'_k}) f'_k(x_{m_k})}{\sum_{m'_k} P'_k(x_{m'_k}) P(\hat{x}_{m''_\mathcal{K}} | x_{m'_k}) f'_k(x_{m'_k})} \tag{43b}$$

$$\geq (1-\rho) \sum_{m_k} \frac{P'_k(x_{m_k}) f'_k(x_{m_k})}{\sum_{m'_k} P'_k(x_{m'_k}) f'_k(x_{m'_k})} \sum_{m''_\mathcal{K}} P(\hat{x}_{m''_\mathcal{K}} | x_{m_k})$$
$$\times \left(1 - \frac{\sum_{m'_k} P'_k(x_{m'_k}) P(\hat{x}_{m''_\mathcal{K}} | x_{m'_k}) f'_k(x_{m'_k})}{\sum_{m'_k} P'_k(x_{m'_k}) P(\hat{x}_{m''_\mathcal{K}} | x_{m'_k}) f'_k(x_{m_k})} \right) \tag{43c}$$

$$= 0, \tag{43d}$$

where $f'_k(x_{m_k}) \triangleq \exp\left(\frac{\rho}{1-\rho} I'_k(x_{m_k}) \right)$ and the equality holds if and only if (41) converges. (42) and (43) together imply $I(x_\mathcal{K}) \geq I'(x_\mathcal{K})$. Since mutual information is bounded above, we conclude the sequence (22) is non-decreasing and convergent in mutual information.

Next, we prove any converging point of sequence (22), denoted as $P_k^\star(x_{m_k})$, fulfills KKT conditions (21). To see this, define

$$D_k^{(r)}(x_{m_k}) \triangleq \frac{P_k^{(r+1)}(x_{m_k})}{P_k^{(r)}(x_{m_k})} = \frac{f_k^{(r)}(x_{m_k})}{\sum_{m'_k} P_k^{(r)}(x_{m'_k}) f_k^{(r)}(x_{m'_k})}. \tag{44}$$

As sequence (22) is convergent, any state with $P_k^\star(x_{m_k}) > 0$ need to satisfy $D_k^\star(x_{m_k}) \triangleq \lim_{r \to \infty} D_k^{(r)}(x_{m_k}) = 1$, namely

$$I_k^\star(x_{m_k}) = \frac{1-\rho}{\rho} \log \sum_{m'_k} P_k^\star(x_{m'_k}) f_k^\star(x_{m'_k}), \tag{45}$$

$$J(P_\mathcal{K}(x_{m_\mathcal{K}}), P'_\mathcal{K}(x_{m_\mathcal{K}})) \triangleq \rho \sum_{m_\mathcal{K}} P_\mathcal{K}(x_{m_\mathcal{K}}) \log \left(1 + \frac{|\boldsymbol{h}_\mathrm{E}^H(x_{m_\mathcal{K}}) \boldsymbol{w}|^2}{\sigma_v^2} \right)$$
$$+ (1-\rho) \sum_{m_\mathcal{K}} P_\mathcal{K}(x_{m_\mathcal{K}}) \sum_{m'_\mathcal{K}} P(\hat{x}_{m'_\mathcal{K}} | x_{m_\mathcal{K}}) \log \frac{P(\hat{x}_{m'_\mathcal{K}} | x_{m_\mathcal{K}}) P'_\mathcal{K}(x_{m_\mathcal{K}})}{P'(\hat{x}_{m'_\mathcal{K}}) P_\mathcal{K}(x_{m_\mathcal{K}})}. \tag{38}$$

which is reminiscent of (35a) and (21a). That is to say, given $P_k^{(0)}(x_{m_k}) > 0$, any converging point with $P_k^\star(x_{m_k}) > 0$ must satisfy (21a). On the other hand, we assume $P_k^\star(x_{m_k})$ does not satisfy (21b), such that for any state with $P_k^\star(x_{m_k}) = 0$,

$$I_k^\star(x_{m_k}) > I^\star(x_{\mathcal{K}}) = \sum_{m_k'} P_k^\star(x_{m_k'}) I_k^\star(x_{m_k'}), \qquad (46)$$

where the equality inherits from (18). Since exponential function is monotonically increasing, we have $f_k^\star(x_{m_k}) > \sum_{m_k'} P_k^\star(x_{m_k'}) f_k^\star(x_{m_k'})$ and $D_k^\star(x_{m_k}) > 1$. Considering $P_k^{(0)}(x_{m_k}) > 0$ and $P_k^\star(x_{m_k}) = 0$, it contradicts with

$$P_k^{(r)}(x_{m_k}) = P_k^{(0)}(x_{m_k}) \prod_{n=1}^{r} D_k^{(n)}(x_{m_k}). \qquad (47)$$

Therefore, given $P_k^{(0)}(x_{m_k}) > 0$, any converging point with $P_k^\star(x_{m_k}) = 0$ must satisfy (21b). This completes the proof.

REFERENCES

[1] C. Boyer and S. Roy, "Backscatter communication and rfid: Coding, energy, and mimo analysis," *IEEE Transactions on Communications*, vol. 62, pp. 770–785, 3 2014. [Online]. Available: http://ieeexplore.ieee.org/document/6685977/

[2] D. Dobkin, *The RF in RFID: Passive UHF RFID in Practice*. Newnes, 11 2012. [Online]. Available: https://www.elsevier.com/books/the-rf-in-rfid/dobkin/978-0-12-394583-9

[3] J. Landt, "The history of rfid," *IEEE Potentials*, vol. 24, pp. 8–11, 10 2005.

[4] G. Vannucci, A. Bletsas, and D. Leigh, "A software-defined radio system for backscatter sensor networks," *IEEE Transactions on Wireless Communications*, vol. 7, pp. 2170–2179, 6 2008. [Online]. Available: http://ieeexplore.ieee.org/document/4543069/

[5] S. D. Assimonis, S. N. Daskalakis, and A. Bletsas, "Sensitive and efficient rf harvesting supply for batteryless backscatter sensor networks," *IEEE Transactions on Microwave Theory and Techniques*, vol. 64, pp. 1327–1338, 4 2016.

[6] V. Liu, A. Parks, V. Talla, S. Gollakota, D. Wetherall, and J. R. Smith, "Ambient backscatter: Wireless communication out of thin air," *ACM SIGCOMM Computer Communication Review*, vol. 43, pp. 39–50, 9 2013. [Online]. Available: https://dl.acm.org/doi/10.1145/2534169.2486015

[7] G. Yang, Q. Zhang, and Y.-C. Liang, "Cooperative ambient backscatter communications for green internet-of-things," *IEEE Internet of Things Journal*, vol. 5, pp. 1116–1130, 4 2018. [Online]. Available: https://ieeexplore.ieee.org/document/8274950/

[8] Y.-C. Liang, Q. Zhang, E. G. Larsson, and G. Y. Li, "Symbiotic radio: Cognitive backscattering communications for future wireless networks," *IEEE Transactions on Cognitive Communications and Networking*, vol. 6, pp. 1242–1255, 12 2020. [Online]. Available: https://ieeexplore.ieee.org/document/9193946/

[9] H. Guo, Y.-C. Liang, R. Long, and Q. Zhang, "Cooperative ambient backscatter system: A symbiotic radio paradigm for passive iot," *IEEE Wireless Communications Letters*, vol. 8, pp. 1191–1194, 8 2019. [Online]. Available: https://ieeexplore.ieee.org/document/8692391/

[10] H. Ding, D. B. da Costa, and J. Ge, "Outage analysis for cooperative ambient backscatter systems," *IEEE Wireless Communications Letters*, vol. 9, pp. 601–605, 5 2020. [Online]. Available: https://ieeexplore.ieee.org/document/8941106/

[11] Q. Zhang, Y.-C. Liang, H.-C. Yang, and H. V. Poor, "Mutualistic mechanism in symbiotic radios: When can the primary and secondary transmissions be mutually beneficial?" *IEEE Transactions on Wireless Communications*, vol. 1276, pp. 1–1, 2022. [Online]. Available: https://ieeexplore.ieee.org/document/9751388/

[12] R. Long, Y.-C. Liang, H. Guo, G. Yang, and R. Zhang, "Symbiotic radio: A new communication paradigm for passive internet of things," *IEEE Internet of Things Journal*, vol. 7, pp. 1350–1363, 2 2020. [Online]. Available: https://ieeexplore.ieee.org/document/8907447/

[13] S. Zhou, W. Xu, K. Wang, C. Pan, M.-S. Alouini, and A. Nallanathan, "Ergodic rate analysis of cooperative ambient backscatter communication," *IEEE Wireless Communications Letters*, vol. 8, pp. 1679–1682, 12 2019. [Online]. Available: https://ieeexplore.ieee.org/document/8807353/

[14] T. Wu, M. Jiang, Q. Zhang, Q. Li, and J. Qin, "Beamforming design in multiple-input-multiple-output symbiotic radio backscatter systems," *IEEE Communications Letters*, vol. 25, pp. 1949–1953, 6 2021. [Online]. Available: https://ieeexplore.ieee.org/document/9358202/

[15] J. Xu, Z. Dai, and Y. Zeng, "Enabling full mutualism for symbiotic radio with massive backscatter devices," *arXiv:2106.05789*, 6 2021. [Online]. Available: http://arxiv.org/abs/2106.05789

[16] H. Yang, H. Ye, K. Liang, and X. Chu, "Energy efficiency maximization for symbiotic radio networks with multiple backscatter devices," *IEEE Open Journal of the Communications Society*, vol. 2, pp. 1431–1444, 2021. [Online]. Available: https://ieeexplore.ieee.org/document/9461158/

[17] S. Han, Y.-C. Liang, and G. Sun, "The design and optimization of random code assisted multi-bd symbiotic radio system," *IEEE Transactions on Wireless Communications*, vol. 20, pp. 5159–5170, 8 2021. [Online]. Available: https://ieeexplore.ieee.org/document/9382925/

[18] X. Xu, Y.-C. Liang, G. Yang, and L. Zhao, "Reconfigurable intelligent surface empowered symbiotic radio over broadcasting signals," vol. 2020-Janua. IEEE, 12 2020, pp. 1–6. [Online]. Available: https://ieeexplore.ieee.org/document/9348236/

[19] M. Hua, Q. Wu, L. Yang, R. Schober, and H. V. Poor, "A novel wireless communication paradigm for intelligent reflecting surface based symbiotic radio systems," *IEEE Transactions on Signal Processing*, vol. 70, pp. 550–565, 4 2022. [Online]. Available: http://arxiv.org/abs/2104.09161https://ieeexplore.ieee.org/document/9652042/

[20] G. Vougioukas and A. Bletsas, "Switching frequency techniques for universal ambient backscatter networking," *IEEE Journal on Selected Areas in Communications*, vol. 37, pp. 464–477, 2 2019. [Online]. Available: https://ieeexplore.ieee.org/document/8474355/

[21] Q. Wu, S. Zhang, B. Zheng, C. You, and R. Zhang, "Intelligent reflecting surface-aided wireless communications: A tutorial," *IEEE Transactions on Communications*, vol. 69, pp. 3313–3351, 5 2021. [Online]. Available: https://ieeexplore.ieee.org/document/9326394/

[22] Q. Wu and R. Zhang, "Intelligent reflecting surface enhanced wireless network: Joint active and passive beamforming design," vol. 18. IEEE, 12 2018, pp. 1–6. [Online]. Available: https://ieeexplore.ieee.org/document/8647620/

[23] S. Zhang and R. Zhang, "Capacity characterization for intelligent reflecting surface aided mimo communication," *IEEE Journal on Selected Areas in Communications*, vol. 38, pp. 1823–1838, 8 2020. [Online]. Available: https://ieeexplore.ieee.org/document/9110912/

[24] S. Lin, B. Zheng, F. Chen, and R. Zhang, "Intelligent reflecting surface-aided spectrum sensing for cognitive radio," *IEEE Wireless Communications Letters*, vol. 11, pp. 928–932, 5 2022.

[25] Y. Liu, Y. Zhang, X. Zhao, S. Geng, P. Qin, and Z. Zhou, "Dynamic-controlled ris assisted multi-user miso downlink system: Joint beamforming design," *IEEE Transactions on Green Communications and Networking*, vol. 6, pp. 1069–1081, 6 2022.

[26] Z. Feng, B. Clerckx, and Y. Zhao, "Waveform and beamforming design for intelligent reflecting surface aided wireless power transfer: Single-user and multi-user solutions," *IEEE Transactions on Wireless Communications*, 2022.

[27] Y. Zhao, B. Clerckx, and Z. Feng, "Irs-aided swipt: Joint waveform, active and passive beamforming design under nonlinear harvester model," *IEEE Transactions on Communications*, vol. 70, pp. 1345–1359, 2022.

[28] Y. Yang, S. Zhang, and R. Zhang, "Irs-enhanced ofdma: Joint resource allocation and passive beamforming optimization," *IEEE Wireless Communications Letters*, vol. 9, pp. 760–764, 6 2020. [Online]. Available: https://ieeexplore.ieee.org/document/8964457/

[29] Q. Wu, X. Zhou, and R. Schober, "Irs-assisted wireless powered noma: Do we really need different phase shifts in dl and ul?" *arXiv:2102.08739*, vol. 10, pp. 1493–1497, 7 2021. [Online]. Available: https://ieeexplore.ieee.org/document/9400380/

[30] Q. Wu, X. Zhou, W. Chen, J. Li, and X. Zhang, "Irs-aided wpcns: A new optimization framework for dynamic irs beamforming," *IEEE Transactions on Wireless Communications*, pp. 1–1, 12 2021.

[31] M. Hua and Q. Wu, "Joint dynamic passive beamforming and resource allocation for irs-aided full-duplex wpcn," *IEEE Transactions on Wireless Communications*, pp. 1–1, 12 2021.

[32] R. Karasik, O. Simeone, M. D. Renzo, and S. S. Shitz, "Beyond max-snr: Joint encoding for reconfigurable intelligent surfaces," vol. 2020-June. IEEE, 6 2020, pp. 2965–2970. [Online]. Available: https://ieeexplore.ieee.org/document/9174060/

[33] H. Chen, G. Yang, and Y.-C. Liang, "Joint active and passive beamforming for reconfigurable intelligent surface enhanced symbiotic radio system," *IEEE Wireless Communications Letters*, vol. 10, pp. 1056–1060, 5 2021. [Online]. Available: https://ieeexplore.ieee.org/document/9345739/

[34] Q. Zhang, Y.-C. Liang, and H. V. Poor, "Reconfigurable intelligent surface assisted mimo symbiotic radio networks," *IEEE Transactions on Communications*, vol. 69, pp. 4832–4846, 7 2021. [Online]. Available: https://ieeexplore.ieee.org/document/9391685/

[35] S. Hu, C. Liu, Z. Wei, Y. Cai, D. W. K. Ng, and J. Yuan, "Beamforming design for intelligent reflecting surface-enhanced symbiotic radio systems," *arxiv:2110.10316*, 10 2021. [Online]. Available: http://arxiv.org/abs/2110.10316

[36] C. Qiu, Q. Wu, M. Hua, X. guan, and Y. Wu, "Achieving multi-beam gain in intelligent reflecting surface assisted wireless energy transfer," *arXiv:2205.08893*, 5 2022. [Online]. Available: http://arxiv.org/abs/2205.08893

[37] Y. Huang, A. Alieldin, and C. Song, "Equivalent circuits and analysis of a generalized antenna system," *IEEE Antennas and Propagation Magazine*, vol. 63, pp. 53–62, 4 2021. [Online]. Available: https://ieeexplore.ieee.org/document/9392844/

[38] J. Kim and B. Clerckx, "Wireless information and power transfer for iot: Pulse position modulation, integrated receiver, and experimental validation," *arXiv:2104.08404*, pp. 1–15, 4 2021. [Online]. Available: http://arxiv.org/abs/2104.08404

[39] C. Boyer and S. Roy, "Coded qam backscatter modulation for rfid," *IEEE Transactions on Communications*, vol. 60, pp. 1925–1934, 7 2012. [Online]. Available: http://ieeexplore.ieee.org/document/6202629/

[40] S. J. Thomas, E. Wheeler, J. Teizer, and M. S. Reynolds, "Quadrature amplitude modulated backscatter in passive and semipassive uhf rfid systems," *IEEE Transactions on Microwave Theory and Techniques*, vol. 60, pp. 1175–1182, 4 2012. [Online]. Available: http://ieeexplore.ieee.org/document/6153042/

[41] D. Bharadia, K. R. Joshi, M. Kotaru, and S. Katti, "Backfi: High throughput wifi backscatter," vol. 45. ACM, 8 2015, pp. 283–296. [Online]. Available: https://dl.acm.org/doi/10.1145/2785956.2787490

[42] G. Yang, C. K. Ho, and Y. L. Guan, "Multi-antenna wireless energy transfer for backscatter communication systems," *IEEE Journal on Selected Areas in Communications*, vol. 33, pp. 2974–2987, 12 2015. [Online]. Available: http://ieeexplore.ieee.org/document/7274644/

[43] H. Guo, Q. Zhang, S. Xiao, and Y.-C. Liang, "Exploiting multiple antennas for cognitive ambient backscatter communication," *IEEE Internet of Things Journal*, vol. 6, pp. 765–775, 2 2019. [Online]. Available: https://ieeexplore.ieee.org/document/8411483/

[44] Q. Wu and R. Zhang, "Intelligent reflecting surface enhanced wireless network via joint active and passive beamforming," *IEEE Transactions on Wireless Communications*, vol. 18, pp. 5394–5409, 11 2019. [Online]. Available: https://ieeexplore.ieee.org/document/8811733/

[45] J. Qian, Y. Zhu, C. He, F. Gao, and S. Jin, "Achievable rate and capacity analysis for ambient backscatter communications," *IEEE Transactions on Communications*, vol. 67, pp. 6299–6310, 9 2019. [Online]. Available: https://ieeexplore.ieee.org/document/8721108/

[46] T. Nguyen and T. Nguyen, "Capacity achieving quantizer design for binary channels," *IEEE Communications Letters*, vol. 25, pp. 759–763, 3 2021. [Online]. Available: https://ieeexplore.ieee.org/document/9247251/

[47] M. Rezaeian and A. Grant, "Computation of total capacity for discrete memoryless multiple-access channels," *IEEE Transactions on Information Theory*, vol. 50, pp. 2779–2784, 11 2004. [Online]. Available: http://ieeexplore.ieee.org/document/1347364/

[48] J. Buhler and G. Wunder, "A note on capacity computation for the discrete multiple access channel," *IEEE Transactions on Information Theory*, vol. 57, pp. 1906–1910, 4 2011. [Online]. Available: https://ieeexplore.ieee.org/document/5730559/

[49] G. J. O. Jameson, "The incomplete gamma functions," *The Mathematical Gazette*, vol. 100, pp. 298–306, 7 2016. [Online]. Available: https://www.cambridge.org/core/product/identifier/S002555721600067X/type/journal_article

[50] X. He, K. Cai, W. Song, and Z. Mei, "Dynamic programming for sequential deterministic quantization of discrete memoryless channels," *IEEE Transactions on Communications*, vol. 69, pp. 3638–3651, 6 2021. [Online]. Available: https://ieeexplore.ieee.org/document/9366549/

[51] T. Nguyen and T. Nguyen, "On thresholding quantizer design for mutual information maximization: Optimal structures and algorithms," vol. 2020-May. IEEE, 5 2020, pp. 1–5. [Online]. Available: https://ieeexplore.ieee.org/document/9128966/

[52] J. Qian, A. N. Parks, J. R. Smith, F. Gao, and S. Jin, "Iot communications with m-psk modulated ambient backscatter: Algorithm, analysis, and implementation," *IEEE Internet of Things Journal*, vol. 6, pp. 844–855, 2 2019. [Online]. Available: https://ieeexplore.ieee.org/document/8423609/

[53] S. Arimoto, "An algorithm for computing the capacity of arbitrary discrete memoryless channels," *IEEE Transactions on Information Theory*, vol. 18, pp. 14–20, 1 1972. [Online]. Available: http://ieeexplore.ieee.org/document/1054753/

[54] R. E. Blahut, "Computation of channel capacity and rate-distortion functions," *IEEE Transactions on Information Theory*, vol. 18, pp. 460–473, 7 1972. [Online]. Available: http://ieeexplore.ieee.org/document/1054855/

[55] E. Calvo, D. P. Palomar, J. R. Fonollosa, and J. Vidal, "On the computation of the capacity region of the discrete mac," *IEEE Transactions on Communications*, vol. 58, pp. 3512–3525, 12 2010. [Online]. Available: http://ieeexplore.ieee.org/document/5590317/